Analysis of Slow-Wave Coplanar Waveguide for Monolithic Integrated Circuits

YOSHIRO FUKUOKA, STUDENT MEMBER, IEEE, YI-CHI SHIH, MEMBER, IEEE, AND TATSUO ITOH, FELLOW, IEEE

Abstract—**The slow-wave characteristics of an MIS coplanar waveguide are analyzed using two different full-wave methods: mode-matching and spectral-domain technique. The theoretical results obtained with them and the experimental values are in good agreement. Several important features of the MIS coplanar waveguide are presented along with some design criteria.**

I. Introduction

MONOLITHIC MICROWAVE integrated circuits (MMIC's) based on gallium arsenide (GaAs) technology are being seriously considered as viable candidates for satellite communication systems, airborne radar systems, and other applications [1], [2]. The dielectric properties of semi-insulating GaAs, combined with the excellent microwave performance of GaAs field-effect transistors (GaAs FET's), make it possible to design monolithic microwave integrated circuits. The monolithic approach provides ease in circuit fabrication without the need to wire bond various components. This reduces the cost of manufacturing and improves reliability and reproducibility.

However, as the physical dimensions of the circuit components become smaller, it becomes difficult to trim and trouble-shoot a working circuit. To minimize this need for trimming, and to achieve design goals, a computer-aided design (CAD) procedure is indeed essential. Another potential problem which arises due to the small chip size is the RF coupling within the circuit. To overcome aforesaid problems, it is necessary to acquire a thorough knowledge of the properties of various planar transmission lines on semiconductor substrates.

On a planar substrate there are basically two different types of transmission lines available. They are microstrip lines and several coplanar structures such as slotline and coplanar waveguide. In the past two decades, they have been studied using various analytical and numerical techniques such as conformal mapping, finite difference, finite element, spectral domain, and so on. Based on the field distributions of these lines and their electrical characteristics, microstrip lines and coplanar waveguides are considered to be the most suitable for MMIC's [3].

Planar metal–insulator–semiconductor (MIS) structures have been investigated by many authors. Simplified parallel plate structures were first examined [4], [5], and the existence of slow-wave propagation was experimentally observed for microstrip lines [5], [6] and coplanar waveguides [7]. This characteristic cannot only be used in delay lines, but, if the insulator layer is replaced by a Schottky contact between the metal and the semiconductor substrate, it can also be used as an electronically controllable variable phase shifter [8]. Some other applications employing these structures have also been proposed in [9].

The purpose of this paper is to present detailed analyses of MIS coplanar waveguides. Previous studies have shown the applicability of several techniques to the analysis of MIS microstrip lines [10]–[12], as well as MIS coplanar waveguides [12]–[15]. However, so far no detailed studies have been reported. The methods employed here include the mode-matching method and the spectral-domain technique. These methods have been used to analyze conventional lossless planar structures, and yield accurate results for the frequency-dependent propagation constants. In the present case, the doped region of the semiconductor substrate is treated as a dielectric layer with a finite resistivity, which is included in the analysis by the complex permittivity for the layer. Several basis functions are needed for both methods to obtain accurate results.

The results of both methods are in good agreement. They also agree well with the experimental results reported in [7]. Some important features of MIS transmission lines are presented in this paper.

II. Method of Analysis: Mode-Matching Method

The mode-matching method has been widely used to analyze microstrip lines [16], as well as dielectric waveguides [17], [18]. This method utilizes the eigenfunction expansion of the field. The cross-sectional view of the structure is shown in Fig. 1. Unlike the spectral-domain technique, the thickness of metallization can be taken into account. Since we are interested in the even dominant mode, a magnetic wall can be placed at $x = 0$, and only the right half of the structure is considered. In order to expand the field in terms of the Fourier series, a hypothetical electric wall needs to be placed at the far right side $x = w$ ($w \gg a$). Since the field is expected to be strongly confined

Manuscript received November, 12, 1982; revised March 1, 1983. This work was supported in part by the Office of Naval Research under Contract N00014-79-0053, in part by the Joint Services Electronics Program under Grant F49620-79-C-0101, and in part by the U.S. Army Research Office under Contract DAAG29-81-K-0053.

Y. Fukuoka and T. Itoh are with the Department of Electrical Engineering, University of Texas at Austin, Austin TX 78712.

Y. C. Shih is with the U.S. Naval Postgraduate School, Monterey, CA 93940.

0018-9480/83/0700-0567$01.00 ©1983 IEEE

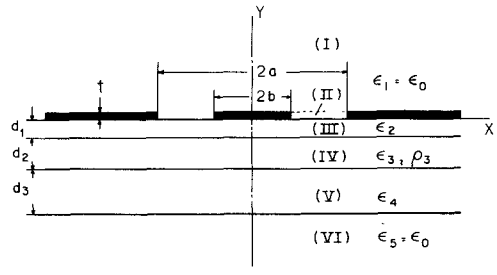

Fig. 1. Cross-sectional view of MIS coplanar waveguide. Region III—insulator layer. Region IV—doped semiconductor layer. Region V —semi-insulating layer. Regions I, II, and VI—air.

in the slot regions, the influence of this hypothetical electric wall is negligible. The cross section is divided into six regions, and the potentials in each region are expanded in terms of eigenfunctions. Since there are many layers in the y-direction, it is preferable to write the electric and magnetic potentials with respect to the y-direction. (This allows the boundary conditions to be easily matched.) The potentials in each region are

$$\psi^1(x,y) = \sum_{n=1}^{M} A_n \cos\beta_n x \exp\left[-\alpha_{1n}(y-t)\right]$$

$$\phi^1(x,y) = \sum_{n=1}^{M} B_n \sin\beta_n x \exp\left[-\alpha_{1n}(y-t)\right]$$

$$\psi^2(x,y) = \sum_{n=2}^{N} \sin\beta_{pn}(x-a) \cdot\{C_{1n}\sin\alpha_{2n}y + C_{2n}\cos\alpha_{2n}y\}$$

$$\phi^2(x,y) = \sum_{n=1}^{N} \cos\beta_{pn}(x-a) \cdot\{D_{1n}\sin\alpha_{2n}y + D_{2n}\cos\alpha_{2n}y\}$$

$$\vdots$$

$$\psi^6(x,y) = \sum_{n=1}^{M} K_n \cos\beta_n x \exp\left[\alpha_{6n}(y+d_1+d_2+d_3)\right]$$

$$\phi^6(x,y) = \sum_{n=1}^{M} L_n \sin\beta_n x \exp\left[\alpha_{6n}(y+d_1+d_2+d_3)\right] \quad (1)$$

where ψ's and ϕ's are the magnetic and electric potentials with respect to the y-direction, respectively. $A_n, B_n, \cdots, L_n$ are coefficients to be determined, and N is the number of basis functions in the slot region and M in the other regions. γ is the complex propagation constant in the z-direction which is to be determined, and the other parameters are

$$\beta_n = (n-0.5)\pi/w$$

$$\beta_{pn} = (n-1)\pi/(b-a)$$

$$\alpha_{1n}^2 = \gamma^2 + \beta_n^2 - \omega^2\epsilon_0\mu_0$$

$$\alpha_{2n}^2 = \omega^2\epsilon_0\mu_0 - \gamma^2 - \beta_{pn}^2$$

$$\vdots$$

$$\alpha_{6n}^2 = \gamma^2 + \beta_n^2 - \omega^2\epsilon_0\mu_0. \quad (2)$$

The field components are then calculated in terms of these potentials with the following equations:

$$\vec{E}(x,y) = -\nabla\times\vec{e}_y\phi - j\omega\mu_0\vec{e}_y\psi + \nabla(\nabla\cdot\vec{e}_y\psi)/j\omega\epsilon$$

$$\vec{H}(x,y) = \nabla\times\vec{e}_y\psi - j\omega\epsilon\vec{e}_y\phi + \nabla(\nabla\cdot\vec{e}_y\phi)/j\omega\mu_0 \quad (3)$$

where $\vec{e}_y$ is a unit vector in the y-direction, and ϵ takes a different value in each region and particularly a complex value in region 4. The potential functions in (1) already satisfy the boundary conditions at the magnetic wall at $x = 0$ and the electric wall at $x = w$, and $x = a$, $x = b$ in the slot region. The remaining boundary conditions are satisfied to yield the following set of homogeneous equations:

$$\sum_{n=2}^{N}(P_{1mn}C_{1n} + P_{2mn}C_{2n}) + \sum_{n=1}^{N}(P_{3mn}D_{1n} + P_{4mn}D_{2n}) = 0, \quad m = 2,3,4,\cdots,N$$

$$\sum_{n=2}^{N}(Q_{1mn}C_{1n} + Q_{2mn}C_{2n}) + \sum_{n=1}^{N}(Q_{3mn}D_{1n} + Q_{4mn}D_{2n}) = 0, \quad m = 1,2,3,\cdots,N$$

$$\sum_{n=2}^{N}(R_{1mn}C_{1n} + R_{2mn}C_{2n}) + \sum_{n=1}^{N}(R_{3mn}D_{1n} + R_{4mn}D_{2n}) = 0, \quad m = 2,3,4,\cdots,N$$

$$\sum_{n=2}^{N}(S_{1mn}C_{1n} + S_{2mn}C_{2n}) + \sum_{n=1}^{N}(S_{3mn}D_{1n} + S_{4mn}D_{2n}) = 0, \quad m = 1,2,3,\cdots,N \quad (4)$$

where P, Q, R, and S are given in the Appendix. Equations (4) can be written in a matrix form

$$ZU = 0 \quad (5)$$

where Z is a square matrix of order $4N-2$, and vector U contains unknown coefficients C_{1n}, C_{2n}, D_{1n}, and D_{2n}. The determinant of the matrix Z is set equal to zero to obtain a nontrivial solution of the vector U, which, at the same time, determines the propagation constant γ.

III. Method of Analysis: Spectral-Domain Technique

The spectral-domain technique has been applied to analyze a number of lossless planar transmission lines [19]–[21]. A simple method for formulating the dyadic Green's functions in the spectral domain, proposed recently by Itoh [19], is based on the transverse equivalent transmission lines. With complex permittivities representing lossy dielectric substrates, this method is followed to analyze the structure (Fig. 1) where the metallic strips are assumed to be infinitesimally thin perfect conductors. The immediate result is the following set of coupled equations:

$$\begin{bmatrix} \tilde{Y}_{xx}(\alpha,\gamma) & \tilde{Y}_{xz}(\alpha,\gamma) \\ \tilde{Y}_{zx}(\alpha,\gamma) & \tilde{Y}_{zz}(\alpha,\gamma) \end{bmatrix} \begin{bmatrix} \tilde{E}_x(\alpha) \\ \tilde{E}_z(\alpha) \end{bmatrix} = \begin{bmatrix} \tilde{J}_x(\alpha) \\ \tilde{J}_z(\alpha) \end{bmatrix} \quad (6)$$

where $\tilde{Y}_{xx}, \tilde{Y}_{xz}, \tilde{Y}_{zx}$, and $\tilde{Y}_{zz}$ are the dyadic Green's functions similar to those derived in [19], and $\tilde{E}_x$, $\tilde{E}_z$, $\tilde{J}_x$, and $\tilde{J}_z$ are the Fourier transform of x and z components of the electric fields and current densities, respectively. α is the

Fourier transform variable and γ is the propagation constant. Following Galerkin's procedure in the spectral domain, we express slot field components $E_x(x)$ and $E_z(x)$ in terms of a complete set of known basis functions

$$E_x(x) = \sum_{n=0}^{N} c_n E_{xn}$$
$$E_z(x) = \sum_{n=0}^{N} d_n E_{zn} \tag{7}$$

where c_n and d_n are unknown coefficients.

The expressions in (7) are Fourier transformed and substituted into (6). The inner products of the resultant equations with each of the basis functions are performed and result in homogeneous linear simultaneous equations. The right-hand side is identically zero by the inner product process [19], [20]. A nontrivial solution may again be obtained by requiring the determinant of the coefficient matrix to be zero; this results in a characteristic equation from which γ is obtained.

Any kind of basis function may be used as long as it is nonzero only in the slot region. However, due to the variational nature of the approach, the efficiency and accuracy of this method depend greatly on the choice of basis functions. In this study, the following sets of basis functions are employed [20]:

$$E_{xn}(x) = \begin{cases} \cos[n\pi x/(b-a)]/\sqrt{\eta^2 - x^2}, & n = 0,2,4,\cdots \\ \sin[n\pi x/(b-a)]/\sqrt{\eta^2 - x^2}, & n = 1,3,5,\cdots \end{cases}$$

$$E_{zn}(x) = \begin{cases} \cos[n\pi x/(b-a)]/\sqrt{\eta^2 - x^2}, & n = 1,3,5,\cdots \\ \sin[n\pi x/(b-a)]/\sqrt{\eta^2 - x^2}, & n = 2,4,6,\cdots \end{cases} \tag{8}$$

where $\eta = (b-a)/2$. Note that these functions are defined only over the slot region. The Fourier transforms of the entire set are

$$\tilde{E}_{xn}(\alpha) = \begin{cases} j\sqrt{\pi/2}\sin[\alpha\xi] \cdot [J_0(r_{n+}) + J_0(r_{n-})], & n = 0,2,4,\cdots \\ -j\sqrt{\pi/2}\cos[\alpha\xi] \cdot [J_0(r_{n+}) - J_0(r_{n-})], & n = 1,3,5,\cdots \end{cases}$$

$$\tilde{E}_{zn}(\alpha) = \begin{cases} \sqrt{\pi/2}\cos[\alpha\xi] \cdot [J_0(r_{n+}) + J_0(r_{n-})], & n = 1,3,5,\cdots \\ \sqrt{\pi/2}\sin[\alpha\xi] \cdot [J_0(r_{n+}) - J_0(r_{n-})], & n = 2,4,6,\cdots \end{cases} \tag{9}$$

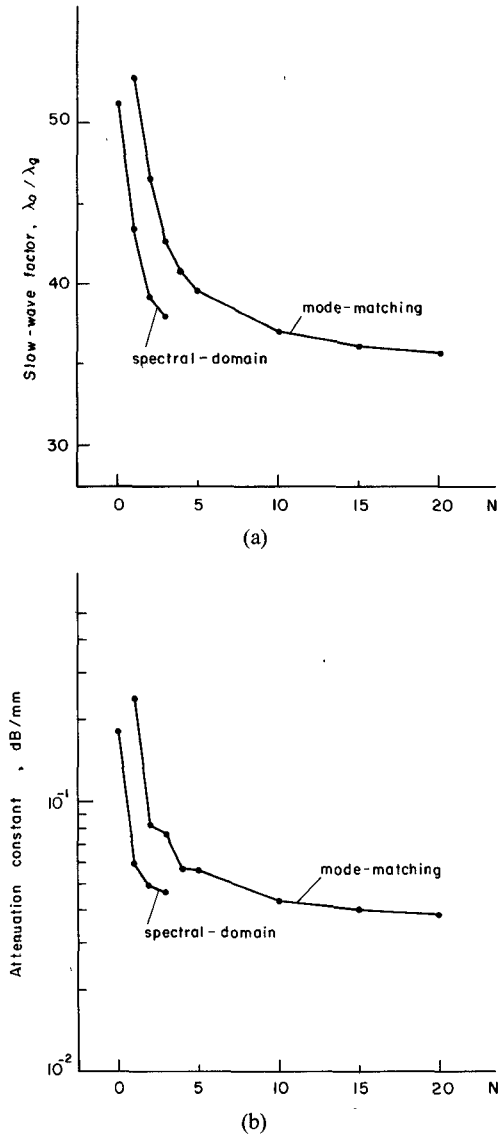

Fig. 2. Convergence of solutions. (a) Slow-wave factor versus frequency. (b) Attenuation constant versus frequency. $a = 50\ \mu$m, $b = 0.5$ mm, $d_1 = 0.4\ \mu$m, $d_2 = 3.0\ \mu$m, $d_3 = 1.0$ mm, $\epsilon_2 = 8.5$, $\epsilon_3 = \epsilon_4 = 13$, $\rho_3 = 0.055$ Ω-mm, $f = 0.1$ GHz, ($t = 1.0\ \mu$m, $w = 1.1$ mm: mode-matching method).

where J_0 denotes the zeroth order Bessel function of the first kind, and

$$\xi = (a+b)/2$$
$$r_{n+} = |(b-a)\alpha + n\pi|/2$$
$$r_{n-} = |(b-a)\alpha - n\pi|/2.$$

IV. Computational Results

In this section, we present numerical results calculated with the analytical procedures described above. The MIS coplanar waveguide structure on GaAs experimentally tested by Hasegawa *et al.* [7] was used to compare the results.

Fig. 2 shows a typical convergence of the numerical results for the slow-wave factors and the attenuation constants. The abscissa is the number of eigenfunctions in region 2 in the mode-matching technique, or the number of basis functions chosen in the spectral-domain method. The rate of convergence strongly depends on the parameters of

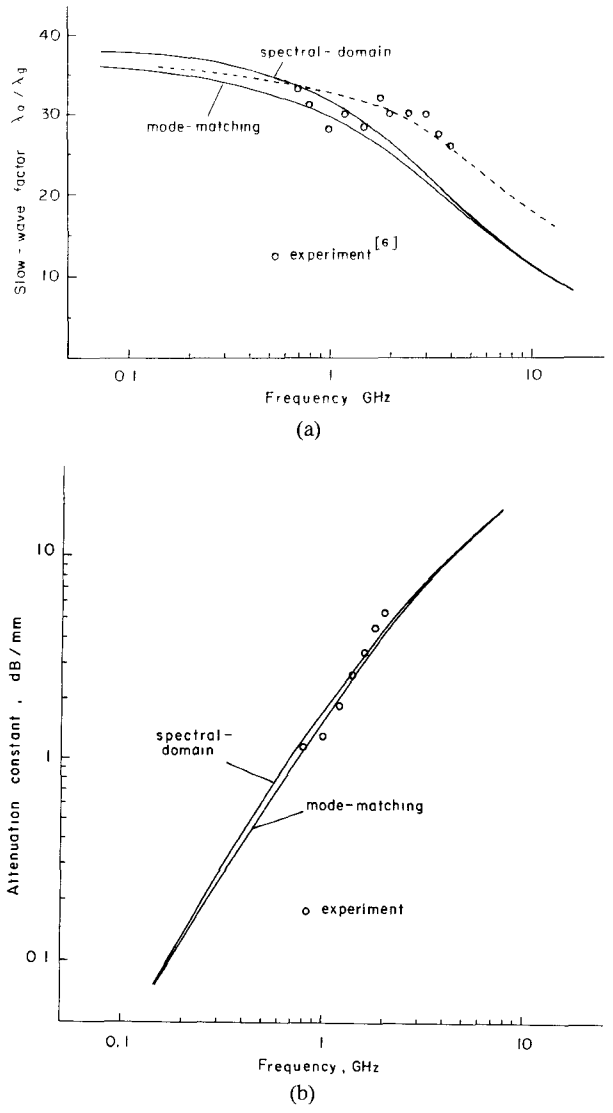

Fig. 3. Comparison of theoretical results with experiment. (a) Slow-wave factor versus frequency. (b) Attenuation constant versus frequency. $a = 50$ μm, $b = 0.5$ mm, $d_1 = 0.4$ μm, $d_2 = 3.0$ μm, $d_3 = 1.0$ mm, $\epsilon_2 = 8.5$, $\epsilon_3 = \epsilon_4 = 13$, $\rho_3 = 0.055$ Ω-mm.

the structure. For this particular structure, it converges slowly. However, faster convergence is achieved with the spectral-domain technique. This is due to the choice of the basis functions for the slot fields. However, for sufficient accuracy, $N = 3$ is not enough for this structure, as seen from Fig. 2. The spectral-domain technique takes up excessive memory size in the computer during numerical integrations involving Bessel functions. Therefore, it is difficult to include more basis functions. On the other hand, the evaluations of the coefficients are fairly easy for the mode-matching method.

Fig. 3 shows the comparison of numerical results obtained by these two methods with the experiment. At higher frequencies, the discrepancy in the results of these two methods is smaller, and the convergence of the solutions is faster. In Fig. 3(a), the experimental results show slower propagation around 2–4 GHz when compared to these theories. A possible reason for this phenomenon is the approximation made to model the doped region (region

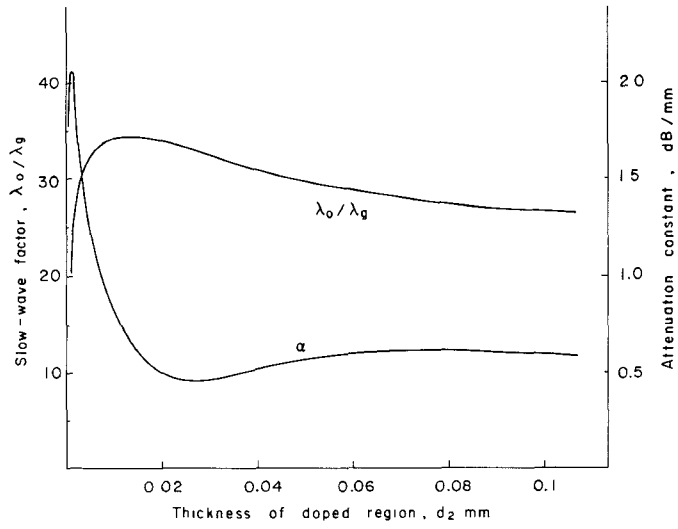

Fig. 4. Propagation characteristics versus thickness of the doped semiconductor region. $a = 50$ μm, $b = 0.5$ mm, $d_1 = 0.4$ μm, $d_2 + d_3 = 1.0$ mm, $\epsilon_2 = 8.5$, $\epsilon_3 = \epsilon_4 = 13$, $\rho_3 = 0.055$ Ω-mm, $f = 1.0$ GHz.

4) of the substrate, which is assumed to be uniformly doped through the depth d_2. If we double d_2, we can obtain a better fit between the theoretical and the experimental results. This is shown by dotted line in Fig. 3(a).

Since this is interesting, we show the behavior of the slow-wave factor and the attenuation constant with respect to the thickness of the doped region in Fig. 4. From now on, the mode-matching method is used for calculations. It should be pointed out that the slow-wave factor has a maximum at a certain value of the thickness, while the attenuation constant has a sharp peak at a very small thickness value and a broad minimum at a moderate thickness value. This phenomenon should be understood in relation to the propagation characteristics with respect to the resistivity of the doped region, which will be discussed later. That is, varying the thickness of the doped region has a similar effect as varying the resistivity. However, the attenuation constant should become large at a small thickness value because the current in the doped region is confined in a very small region. This may be an important feature from a design point of view. As one might expect, both slow-wave factor and attenuation constant approach to constant values as the thickness of the doped region increases.

Another interesting parameter is the thickness d_1 of the insulator region (region 3). If a Schottky-contact coplanar waveguide, used as a variable phase shifter, is approximated by a MIS coplanar line, and its electrical tunability is to be evaluated, the most important parameter is d_1, which is analogous to the thickness of the depletion layer. Several curves in Fig. 5 show almost linear relationship between the slow-wave factor and the thickness d_1. The slope of the curve strongly depends on the frequency. At a lower frequency, the propagation constant has greater dependence on d_1. At higher frequency, such as $f = 5$ GHz, the slow-wave factor is not affected by the change in thickness d_1. This is attributed to the fact that the waveguide is not being operated in the slow-wave region.

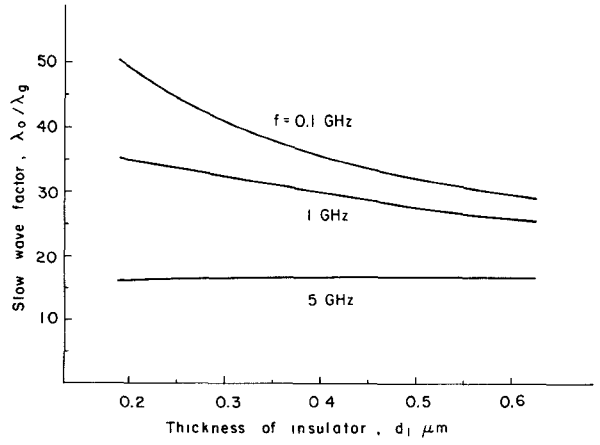

Fig. 5. Slow-wave factor versus thickness of the insulator region. $a = 50$ μm, $b = 0.5$ mm, $d_2 = 3.0$ μm, $d_3 = 1.0$ mm, $\epsilon_2 = 8.5$, $\epsilon_3 = \epsilon_4 = 13$, $\rho_3 = 0.055$ Ω-mm.

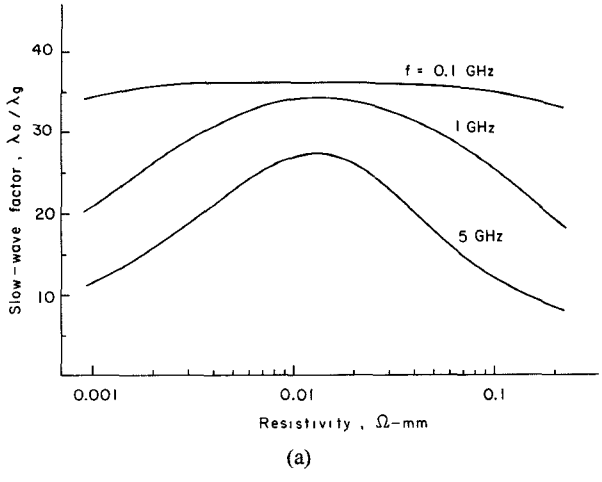

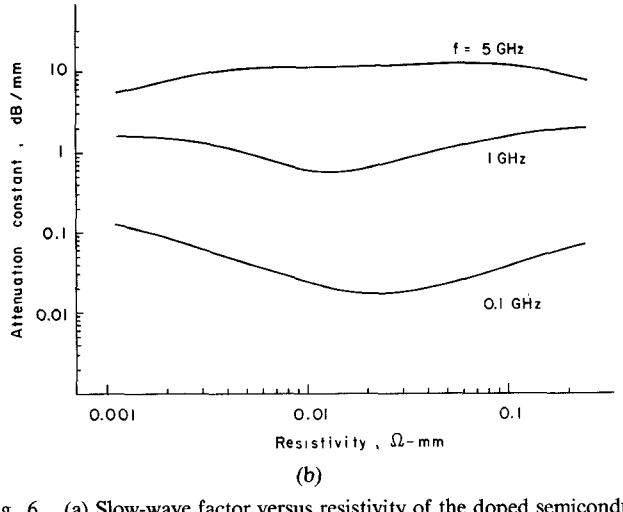

Fig. 6. (a) Slow-wave factor versus resistivity of the doped semiconductor region. (b) Attenuation constant versus resistivity of the doped semiconductor region. $a = 50$ μm, $b = 0.5$ mm, $d_1 = 0.4$ μm, $d_2 = 3.0$ μm, $d_3 = 1.0$ mm, $\epsilon_2 = 8.5$, $\epsilon_3 = \epsilon_4 = 13$.

The propagation characteristics as a function of the resistivity of the doped region shows behavior similar to that predicted for MIS microstrip lines [5]. There are basically three operating regions: the slow-wave region, the skin-effect region, and the lossy-dielectric region. Fig. 6(a)

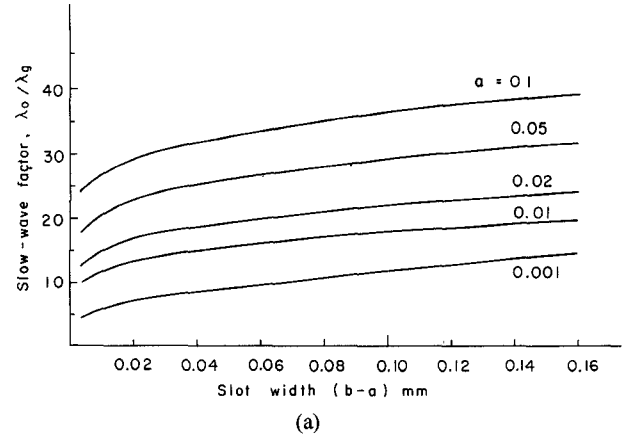

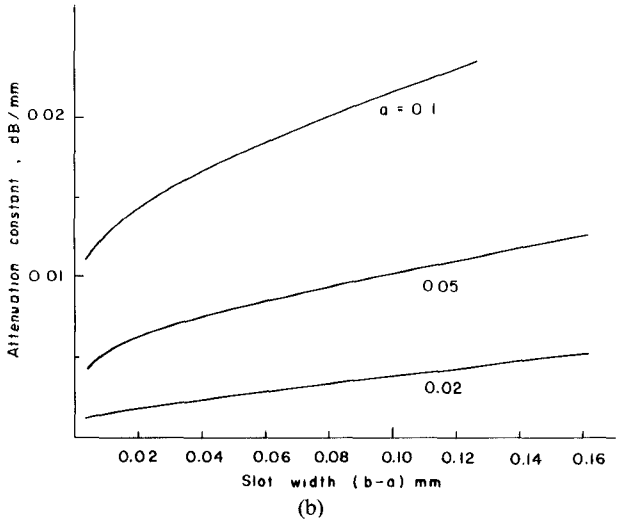

Fig. 7. (a) Slow-wave factor versus slot width. (b) Attenuation constant versus slot width. $d_1 = 0.4$ μm, $d_2 = 3.0$ μm, $d_3 = 1.0$ mm, $\epsilon_2 = 8.5$, $\epsilon_3 = \epsilon_4 = 13$, $\rho_3 = 0.01$ Ω-mm, $f = 0.1$ GHz.

shows a typical behavior of the slow-wave factor for various frequencies. It is observed that there exists an optimum resistivity in the middle of the slow-wave region where the attenuation constant has a local minimum (Fig. 6(b)). The location of this point may be important for applications since the slow-wave factor also has its maximum value at this resistivity value.

Finally, the behavior of the propagation constant due to variations in some other structural parameters is also investigated. For example, the values of the slow-wave factor and the attenuation constant in the slow-wave mode are plotted as a function of slot width in Fig. 7. $f = 0.1$ GHz and $\rho_3 = 0.01$ Ω-mm were chosen so that the coplanar waveguide operates in a slow-wave region. From Fig. 7(a), we observe that the value of the slow-wave factor increases as the width of either the center strip or the slot increases. This behavior may be understood by considering the capacitance of the waveguide. In the slow-wave region, the electric field of the waveguide sees the doped region as a conductor [5]. Therefore, when the width of the center strip increases, the line capacitance increases. When the slot becomes wider, the electric field near the slot spreads out and causes field lines to enter more into the surface of the doped region. This again increases the capacitance. All

these contribute to slower propagation of the wave. Since the wider width of the center strip or slot pushes more energy into the lossy substrate, the attenuation constant shows an increase as shown in Fig. 7(b).

V. Conclusions

MIS coplanar waveguide has been analyzed with two different methods. The conductive semiconductor substrate was treated by a complex permittivity, and the final solution was obtained by searching a complex root of the determinantal equation. The convergence study was successful and the methods employed show good correlation for the propagation constant. The results showed basically similar behavior of the MIS coplanar waveguide to the MIS microstrip line. Some important parameters, such as the thickness and the resistivity of the doped semiconductor layer governing the performance of a MIS coplanar waveguide for practical design of a circuit, were also shown.

Appendix

The coefficients appearing in (4) are given by

$$P_{1mn} = h_{1mn}\cos\alpha_{pn}t - \delta_{mn}[w(b-a)/4]\gamma\sin\alpha_{pm}t$$

$$P_{2mn} = -h_{1mn}\sin\alpha_{pn}t - \delta_{mn}[w(b-a)/4]\gamma\cos\alpha_{pm}t$$

$$P_{3mn} = h_{2mn}\sin\alpha_{pn}t - \delta_{mn}[w(b-a)/4](1/\omega\mu_0)\alpha_{pm}\beta_{pm}\cos\alpha_{pm}t$$

$$P_{4mn} = h_{2mn}\cos\alpha_{pn}t + \delta_{mn}[w(b-a)/4](1/\omega\mu_0)\alpha_{pm}\beta_{pm}\sin\alpha_{pm}t$$

$$Q_{1mn} = k_{1mn}\cos\alpha_{pn}t - \delta_{mn}[w(b-a)/4](1+\delta_{mo})\beta_{pm}\sin\alpha_{pm}t$$

$$Q_{2mn} = -k_{1mn}\sin\alpha_{pn}t - \delta_{mn}[w(b-a)/4](1+\delta_{mo})\beta_{pm}\cos\alpha_{pm}t$$

$$Q_{3mn} = k_{2mn}\sin\alpha_{pn}t + \delta_{mn}[w(b-a)/4](1+\delta_{mo})(\gamma/\omega\mu_0)\alpha_{pm}\cos\alpha_{pm}t$$

$$Q_{4mn} = k_{2mn}\cos\alpha_{pn}t - \delta_{mn}[w(b-a)/4](1+\delta_{mo})(\gamma/\omega\mu_0)\alpha_{pm}\sin\alpha_{pm}t$$

$$R_{1mn} = \sum_{s=1}^{N}[\gamma/(\beta_s^2+\gamma^2)]\{-(\epsilon_2/\epsilon_1\alpha_{2s})(E_{2s}/E_{1s})T_{sn}^1 - (\alpha_{2s}\beta_s/\omega\epsilon_1)(F_{1s}/F_{2s})T_{sn}^2\}A_{ms}^s\alpha_{pn}$$

$$R_{2mn} = -\delta_{mn}[w(b-a)/4]\gamma$$

$$R_{3mn} = -\delta_{mn}[w(b-a)/4](1/\omega\mu_0)\alpha_{pm}\beta_{pm}$$

$$R_{4mn} = \sum_{s=1}^{N}[1/(\beta_s^2+\gamma^2)]\{-(\gamma^2\omega\epsilon_2/\alpha_{2s})(E_{2s}/E_{1s})T_{sn}^3 - \alpha_{2s}\beta_s(F_{1s}/F_{2s})T_{sn}^4\}A_{ms}^s$$

$$S_{1mn} = \sum_{s=1}^{N}[1/(\beta_s^2+\gamma^2)]\{(\epsilon_2\beta_s/\epsilon_1\alpha_{2s})(E_{2s}/E_{1s})T_{sn}^1 - \gamma^2(\alpha_{2s}/\omega\epsilon_1)(F_{1s}/F_{2s})T_{sn}^2\}A_{ms}^s\alpha_{pn}$$

$$S_{2mn} = -\delta_{mn}[w(b-a)/4](1+\delta_{mo})\beta_{pm}$$

$$S_{3mn} = \delta_{mn}[w(b-a)/4](1+\delta_{mo})(\gamma/\omega\mu_0)\alpha_{pm}$$

$$S_{4mn} = \sum_{s=1}^{N}[\gamma/(\beta_s^2+\gamma^2)]\{(\beta_s\omega\epsilon_2/\alpha_{2s})(E_{2s}/E_{1s})T_{sn}^3 - \alpha_{2s}(F_{1s}/F_{2s})T_{sn}^4\}A_{ms}^s$$

where δ_{mn} is the Kronecker delta function, and the ratios of the coefficients E_{2s}/E_{1s} and F_{1s}/F_{2s} are calculated from the boundary conditions at $y = -d_1$, $-d_1-d_2$, and $-d_1-d_2-d_3$. The other coefficients appearing here are given by

$$h_{1mn} = \sum_{s=1}^{N}[\gamma/(\beta_s^2+\gamma^2)]\cdot\{(1/\alpha_{1s})T_{sn}^1 + (\alpha_{1s}\beta_s/\omega\epsilon_1)T_{sn}^2\}A_{ms}^c\alpha_{pn}$$

$$h_{2mn} = \sum_{s=1}^{N}[1/(\beta_s^2+\gamma^2)]\{(\gamma^2\omega\epsilon_1/\alpha_{1s})T_{sn}^3 + \alpha_{1s}\beta_s T_{sn}^4\}A_{ms}^c$$

$$k_{1mn} = \sum_{s=1}^{N}[1/(\beta_s^2+\gamma^2)]\cdot\{-(\beta_s/\alpha_{1s})T_{sn}^1 + (\alpha_{1s}\gamma^2/\omega\epsilon_1)T_{sn}^2\}A_{ms}^s\alpha_{pn}$$

$$k_{2mn} = \sum_{s=1}^{N}[\gamma/(\beta_s^2+\gamma^2)]\{-(\beta_s\omega\epsilon_1/\alpha_{1s})T_{sn}^3 + \alpha_{1s}T_{sn}^4\}A_{ms}^s$$

$$T_{sn}^1 = \beta_s\beta_{pn}A_{ns}^s - \gamma^2A_{ns}^c$$

$$T_{sn}^2 = (1/\omega\mu_0)\{\beta_{pn}A_{ns}^s + \beta_sA_{ns}^c\}$$

$$T_{sn}^3 = \beta_sA_{ns}^s + \beta_{pn}A_{ns}^c$$

$$T_{sn}^4 = (1/\omega\mu_0)\{\gamma^2A_{ns}^s - \beta_s\beta_{pn}A_{ns}^c\}$$

$$A_{ns}^s = \int_a^b \cos\beta_{pn}(x-a)\sin\beta_s x\,dx$$

$$A_{ns}^c = \int_a^b \sin\beta_{pn}(x-a)\cos\beta_s x\,dx$$

References

[1] F. J. Moncrief, "Monolithic MIC's gain momentum as GaAs MSI nears," *Microwaves*, vol. 18, no. 7, pp. 42–53, July 1979.

[2] H. Q. Tserng, "Advance in microwave GaAs power FET device and circuit technologies," in *11th Eur. Microwave Conf.*, Sept. 1981, pp. 48–58.

[3] R. A. Pucel, "Design considerations for monolithic microwave circuits," *IEEE Trans. Microwave Theory Tech.*, vol. MTT-29, pp. 513–534, June 1981.

[4] H. Guckel, P. A. Brennan, and I. Palócz, "A parallel-plate waveguide approach to microminiaturized, planar transmission lines for integrated circuits," *IEEE Trans. Microwave Theory Tech.*, vol. MTT-15, pp. 468–476, Aug. 1967.

[5] H. Hasegawa, M. Furukawa, and H. Yanai, "Properties of microstrip line on Si-SiO_2 system," *IEEE Trans. Microwave Theory Tech.*, vol. MTT-19, pp. 869–881, Nov. 1971.

[6] D. Jäger and W. Rabus, "Bias dependent phase delay of Schottky-contact microstrip lines," *Electron. Lett.*, vol. 9, no. 9, pp. 201–203, May 1973.

[7] H. Hasegawa and H. Okizaki, "M.I.S. and Schottky slow-wave coplanar striplines on GaAs substrates," *Electron. Lett.*, vol. 13, no. 22, pp. 663–664, Oct. 1977.

[8] J. M. Jaffe, "A high frequency variable delay line," *IEEE Trans. Electron Devices*, vol. ED-19, pp. 1292–1294, Dec. 1972.

[9] G. W. Hughes and R. M. White, "Microwave properties of nonlinear MIS and Schottky barrier microstrip," *IEEE Trans. Electron Devices*, vol. ED-22, pp. 945–956, Oct. 1975.
[10] P. Kennis and L. Faucon, "Rigorous analysis of planar MIS transmission lines," *Electron. Lett.*, vol. 17, no. 13, pp. 454–456, June 1981.
[11] M. Aubourg, J. P. Villotte, F. Codon, and Y. Garault, "Analysis of microstrip line on semiconductor substrate," in *IEEE MTT-S Int. Microwave Symp. Dig.*, June 1981, pp. 495–497.
[12] P. Kennis *et al.*, "Properties of microstrip and coplanar lines on semiconductor substrates," in *Proc. 12th Eur. Microwave Conf.*, Sept. 1982, pp. 328–333.
[13] Y.-C. Shih and T. Itoh, "Analysis of printed transmission lines for monolithic integrated circuits," *Electron. Lett.*, vol. 18, no. 14, pp. 585–586, July 1982.
[14] Y. Fukuoka and T. Itoh, "Analysis of slow-wave phenomena in coplanar waveguide on a semiconductor substrate," *Electron. Lett.*, vol. 18, no. 14, pp. 589–590, July 1982.
[15] R. Sorrentino and G. Leuzzi, "Full-wave analysis of integrated transmission lines on layered lossy media," *Electron. Lett.*, vol. 18, no. 14, pp. 607–609, July 1982.
[16] G. Kowalski and R. Pregla, "Dispersion characteristics of shielded microstrips with finite thickness," *Arch. Elek. Übertragung*, vol. 25, no. 4, pp. 193–196, Apr. 1971.
[17] K. Solbach and I. Wolff, "The electromagnetic fields and the phase constants of dielectric image lines," *IEEE Trans. Microwave Theory Tech.*, vol. MTT-26, pp. 266–274, Apr. 1978.
[18] R. Mittra, Y. L. Hou, and V. Jamnejad, "Analysis of open dielectric waveguides using mode-matching technique and variational methods," *IEEE Trans. Microwave Theory Tech.*, vol. MTT-28, pp. 36–43, Jan. 1980.
[19] T. Itoh, "Spectral-domain immittance approach for dispersion characteristics of generalized printed transmission lines," *IEEE Trans. Microwave Theory Tech.*, vol. MTT-28, pp. 733–736, July 1980.
[20] L.-P. Schmidt and T. Itoh, "Spectral-domain analysis of dominant and higher order modes in fin-lines," *IEEE Trans. Microwave Theory Tech.*, vol. MTT-28, pp. 981–985, Sept. 1980.
[21] J. B. Knorr and K.-D. Kuchler, "Analysis of coupled slots and coplanar strips on dielectric substrate," *IEEE Trans. Microwave Theory Tech.*, vol. MTT-23, pp. 541–548, July 1975.

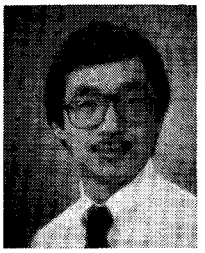

Yoshiro Fukuoka (S'82) was born in Osaka, Japan, on October 11, 1956. He received the B.S. and M.S. degrees in electrical engineering from the University of Electro-Communications, Tokyo, Japan, in 1979 and 1981, respectively. He is currently studying toward the Ph.D. degree at the University of Texas at Austin. His current interest is on the monolithic microwave integrated circuits and components.

Mr. Fukuoka is a member of the Institute of Electronics and Communication Engineers of Japan.

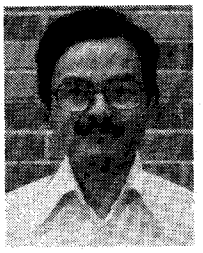

Yi-Chi Shih (SM'80) was born in Taiwan, the Republic of China, on February 8, 1955. He received the B. Eng. degree from National Taiwan University, Taiwan, R.O.C., in 1976, and the M.Sc. degree from the University of Ottawa, Ontario, Canada, in 1980, both in electrical engineering. Since 1980 he has been working toward the Ph.D. degree at The University of Texas at Austin.

His research interest includes the analysis and design of microwave and millimeter-wave components.

Tatsuo Itoh (S'69–M'69–SM'74–F'82) received the Ph.D. degree in electrical engineering from the University of Illinois, Urbana, in 1969.

From September 1966 to April 1976 he was with the Electrical Engineering Department, University of Illinois. From April 1976 to August 1977 he was a Senior Research Engineer in the Radio Physics Laboratory, SRI International, Menlo Park, CA. From August 1977 to June 1978 he was an Associate Professor at the University of Kentucky, Lexington. In July 1978 he joined the faculty at The University of Texas at Austin, where he is now a Professor of Electrical Engineering and Director of the Microwave Laboratory. During the summer 1979, he was a Guest Researcher at AEG-Telefunken, Ulm, West Germany.

Dr. Itoh is a member of the Institute of Electronics and Communication Engineers of Japan, Sigma Xi, and Commissions B and C of USNC/URSI. He is a Professional Engineer registered in the State of Texas.